X-ray simulations with gVXR as a useful tool for education, data analysis, set-up of CT scans, and scanner development

Franck Vidal, Shaghayegh Afshari, Sharif Ahmed, Carolyn Atkins, Eric Béchet, Alberto Corbi Bellot, Stefan Bosse, Younes Chahid, Cheng-Ying Chou, Robert Culver, et al.

X-ray simulations with gVXR as a useful tool for education, data analysis, set-up of CT scans, and scanner development

Franck P. Vidal[a,b], Shaghayegh Afshari[c], Sharif Ahmed[d], Carolyn Atkins[e], Éric Béchet[f], Alberto Corbí Bellot[g], Stefan Bosse[h,i], Younes Chahid[e], Cheng-Ying Chou[c], Robert Culver[j], Lewis Dixon[b], Johan Friemann[k], Amin Garbout[l], Clémentine Hatton[m], Audrey Henry[m], Christophe Leblanc[f], Alberto Leonardi[d], Jean Michel Létang[n], Harry Lipscomb[l], Tristan Manchester[d], Bas Meere[o], Simon Middleburgh[b], Iwan Mitchell[b], Liam Perera[d], Martí Puig[p,l], and Jenna Tugwell-Allsup[q]

[a]Scientific Computing, Ada Lovelace Centre, Science Technology Facilities Council, UK
[b]School of Computer Science & Engineering, Bangor University, UK
[c]Department of Biomechatronics Engineering, National Taiwan University, Taiwan
[d]DIAD beamline, Diamond Light Source, UK
[e]UK Astronomy Technology Centre, Royal Observatory, Edinburgh, UK
[f]Département d'Aérospatiale et Mécanique, Université de Liège, Belgium
[g]Escuela Superior de Ingeniería y Tecnología - Universidad Internacional de La Rioja, Spain
[h]Department of Computer Science, University of Koblenz, Koblenz, Germany
[i]Department of Mechanical Engineering, University of Siegen, Siegen, Germany
[j]The Manufacturing Technology Centre, UK
[k]Department of Industrial and Materials Science, Chalmers University of Technology, Sweden
[l]Henry Royce Institute, Henry Moseley X-ray Imaging Facility, Department of Materials, The University of Manchester, UK
[m]Scalian DS, Rennes, France
[n]INSA-Lyon, Université Claude Bernard Lyon 1, CNRS, Inserm, CREATIS UMR 5220, U1294, Lyon, France
[o]Department of Mechanical Engineering, Eindhoven University of Technology, Netherlands
[p]Department of Engineering Science, University of Oxford, UK
[q]Radiology Department, Betsi Cadwaladr University Health Board (BCUHB), Ysbyty Gwynedd, UK

ABSTRACT

gVirtualXray (gVXR) is an open-source framework that relies on the Beer-Lambert law to simulate X-ray images in real time on a graphics processor unit (GPU) using triangular meshes. A wide range of programming languages is supported (C/C++, Python, R, Ruby, Tcl, C#, Java, and GNU Octave). Simulations generated with gVXR have been benchmarked with clinically realistic phantoms (i.e. complex structures and materials) using Monte Carlo (MC) simulations, real radiographs and real digitally reconstructed radiographs (DRRs), and X-ray computed tomography (CT). It has been used in a wide range of applications, including real-time medical simulators, proposing a new densitometric radiographic modality in clinical imaging, studying noise removal techniques in fluoroscopy, teaching particle physics and X-ray imaging to undergraduate students in engineering, and XCT to masters students, predicting image quality and artifacts in material science, etc. gVXR has also been used to produce a high number of realistic simulated images in optimization problems and to train machine learning algorithms. This paper presents applications of gVXR related to XCT.

Keywords: X-ray imaging, Computed tomography, Simulation, GPU programming, Digital twinning

Further author information: (Send correspondence to F.P.V.)
F.P.V.: E-mail: franck.vidal@stfc.ac.uk

1. INTRODUCTION

The simulation of accurate and fast X-ray images remains a challenge. State-of-the-art Monte Carlo (MC) methods can mimic the physics, by tracking photons as they travel from the source, through matter, to the detector. The computational cost makes it prohibitive in many applications where speed is a requirement, e.g. interactive virtual reality (VR) or high data throughput support. However, it is possible to trade off some of the physical effects such as scattering to speed-up computations, whilst retaining a high level of accuracy.

In Section 2, we describe an open-source framework called gVirtualXray (gVXR). No proprietary technology is used, making it portable and deployable on a wide range of hardware and software platforms. gVXR implements a deterministic simulation model based on the Beer-Lambert law to generate noise-free images. They can provide a good compromise between speed and accuracy[1] and can be implemented on graphics processor units (GPUs) for a further increase of speed.[2,3] Unlike Monte Carlo methods, deterministic simulations tend to ignore scattering and noise. In gVXR, the latter is added as a post-process. The software has been quantitatively tested and validated against MC and experimental data (see Section 3) We also show how it has been deployed in a broad range of applications in various scientific contexts (see Section 4).

2. DESCRIPTION

gVXR is an open-source application programming interface (API) written in C++ to compute the Beer-Lambert law, also known as the attenuation law. If scattering is neglected and an ideal (i.e. Dirac) point-spread function is assumed, X-ray projections $\mathbf{I}(x, y)$ can simply be modeled with the Beer-Lambert attenuation law:

$$\mathbf{I}(x,y) = \sum_i \mathbf{R}(E_i)\,\mathbf{D}(E_i)\ \exp\left(-\sum_j \mu_j(E_i)\ \mathbf{d}_j(x,y)\right) \tag{1}$$

$\mathbf{I}(x, y)$ is the integrated energy in electronvolt (eV), keV or MeV, units of energy commonly used in atomic and nuclear physics, received by pixel (x, y). The beam spectrum emitted by the X-ray source is discretized in several energy channels in the polychromatic case. E_i corresponds to the energy of the i-th energy channel. $\mathbf{D}(E_i)$ is the number of photons emitted by the source at that energy E_i. When the source is monochromatic, e.g. in the case of synchrotron radiation, a single energy channel is used. The detector response $\mathbf{R}(E_i)$ mimics the use of a scintillator by replacing the incident energy E_i with a smaller value, i.e. $\mathbf{R}(E_i) < E_i$. The detector response is assumed space-invariant in Equation 1. j indicates the j-th material being scanned when a multi-material "object" is considered. $\mu_j(E_i)$ is the linear attenuation coefficient in cm^{-1} of the j-th material at energy E_i. $\mathbf{d}_j(x, y)$ is the path length in cm of the ray from the X-ray source to pixel (x, y) crossing the j-th material.

Polygon meshes, e.g. triangles, are used in gVXR to represent 3D objects. This method is commonly used in computer graphics (CG), including real-time video games and VR, animations, and computer-aided design (CAD). It is intuitive to compute the Beer-Lambert law with ray-tracing when polygon meshes are used. However, this technique is relatively computationally intensive: i) a ray must be fired between the source and each detector pixel, and ii) intersection tests for each ray for each triangle of each 3D object must be performed. Freud et al. adapted the Z-buffer technique to efficiently compute $\mathbf{d}_j$ in Eq. 1 from polygon meshes.[4] It relies on rasterization and does not require to sort intersections. In this case, each polygon is processed a single time, projecting it on the detector plane, and using an accumulator buffer. The computational complexity is considerably reduced.

gVXR implements Freud's algorithm on GPU using a graphics API.[2] Since its inception, functionalities have been added to gVXR to improve the level of realism of the simulations. A monochromatic source was initially used to mimic fluoroscopy in a real-time medical VR simulator.[5] Polychromatism and the focal spot of the detector were then introduced to improve realism.[6] In 2013, the code was redeveloped to become, gVXR, and was made available to the community as an open-source project on SourceForge (https://sourceforge.net/projects/gvirtualxray/, accessed: 18 Jul 2024).[3] The impulse response of the detector and Poisson noise are also supported.[7] The scintillator material of the detector and the tube voltage and beam filtration can now be specified.[8]

gVXR is cross-platform: it runs on Windows, GNU/Linux, and MacOS computers (Intel architecture only, although ARM support is planned). It supports GPUs from any manufacturer. gVXR is scalable: it runs

on laptops, desktop PCs, supercomputers, and cloud infrastructures. Containerization using Docker is even possible.[9] A wide range of programming languages (C/C++, Python, R, Ruby, Tcl, C#, Java, and GNU Octave) can be used. Its Python package is available on the Python Package Index (https://pypi.org/project/gVXR/, accessed: 18 Jul 2024).

Surface meshes (triangles) in most popular file formats (eg. STL, PLY, 3DS, OBJ, DXF, X3D, DAE) can be used to define the geometry of scanned objects. Volume meshes (tetrahedrons) in the Abacus format may also be used but their support is experimental. The material property must be specified for each scanned object. Chemical elements (e.g. the symbol 'W' or the atomic number 74 for tungsten); compounds, e.g. H_2O for water; mixtures, e.g. Titanium-aluminum-vanadium alloy, Ti90Al6V4; and Hounsfield units (for medical applications) are supported. The photon cross-sections provided by Xraylib[10] (https://github.com/tschoonj/xraylib, accessed: 18 Jul 2024) are used to compute μ values in Eq. 1.

Cone beam geometries (both point sources and focal spots) are supported to mimic X-ray tubes. A parallel beam can be used for synchrotrons. The beam spectrum can be either monochromatic or polychromatic. Both SpekPy[11] and Xpecgen[12] are supported as backends to specify the tube voltage and the beam filtration used. To increase realism, photonic noise can be turned on. In this case, the photon flux must be specified.

It is possible to model ideal detectors as well as realistic detectors. In this case, the user can specify a point spread function (PSF), i.e. the level of blur inherent to the detector, and the thickness and material composition of the scintillator. It is also possible to simulate spectral imaging.

Orbital, helical and arbitrary trajectories can be supported to simulate a CT acquisition. It is possible to describe the simulation and CT acquisition in Python (or any other supported programming languages) or using a user-friendly JSON file that is loaded from the Python code. Full examples of CT simulation with gVXR and CT reconstruction with CIL[13] are available as Jupyter notebooks on GitHub (https://github.com/TomographicImaging/gVXR-SPIE2024).

3. VALIDATION

To validate the accuracy of gVXR, successive validation tests of increasing complexity were performed. Each milestone was validated individually with an appropriate methodology. For the Beer-Lambert implementation, we initially compared simple images simulated with gVXR with corresponding images simulated with a state-of-the-art Monte Carlo package (Geant4/Gate).[3]

More advanced functionalities, such as voltage, beam filtration and scintillation, were validated using two anthropomorphic phantoms. The first one is a digital phantom: pEdiatRic dosimetRy personalized platfORm (ERROR).[14] It corresponds to the anatomy of a 5-year-old boy. It is provided as a labeled $512 \times 511 \times 190$ volume, which includes 24 different structures, such as air, muscle, bone, stomach-interior, cartilage, etc. As it is a digital phantom, it can be used to compare gVXR and Gate's simulations. The number of photons impinging the detector was 10^9. About 10 days of computations were required on the test computer to produce a simulated image of 128×128 pixels with Gate; only a few microseconds gVXR. Both simulations are visually close. All the image comparison metrics indicate that the images are extremely similar when scattering is ignored: Zero-mean normalised cross-correlation (ZNCC) is 99.99%; mean absolute percentage error (MAPE) is 2.23%, and structural similarity index (SSIM) is 0.99.

The second phantom is the Lungman anthropomorphic chest phantom (Kyoto Kagaku, Tokyo, Japan).[15] It represents a 70 kg male. The phantom is made of materials with X-ray absorption properties close to those of human tissue. Tumors of various densities are embedded. A computed tomography (CT) scan of the phantom was acquired with a device clinically utilized at Ysbyty Gwynedd Hospital (UK), a 128-slice Somatom Definition Edge scanner by Siemens Healthcare (Erlangen, Germany). A digital phantom was first created by image segmentation using open-source toolkits, the Insight Toolkit (ITK)[16] and Visualization Toolkit (VTK).[17] The digital phantom is freely available on Zenodo.[18] The material composition of each segmented structure is derived from the average Hounsfiled unit of the structure in the original CT scan. Schneider et al.[19]'s method is built in gVXR to convert the Hounsfield values into material compositions and densities. A CT scan acquisition is then simulated using gVXR and reconstructed with CIL.[13] The original CT scan taken with the Somatom Definition Edge scanner can be compared with CT volume reconstructed from simulated data. Corresponding

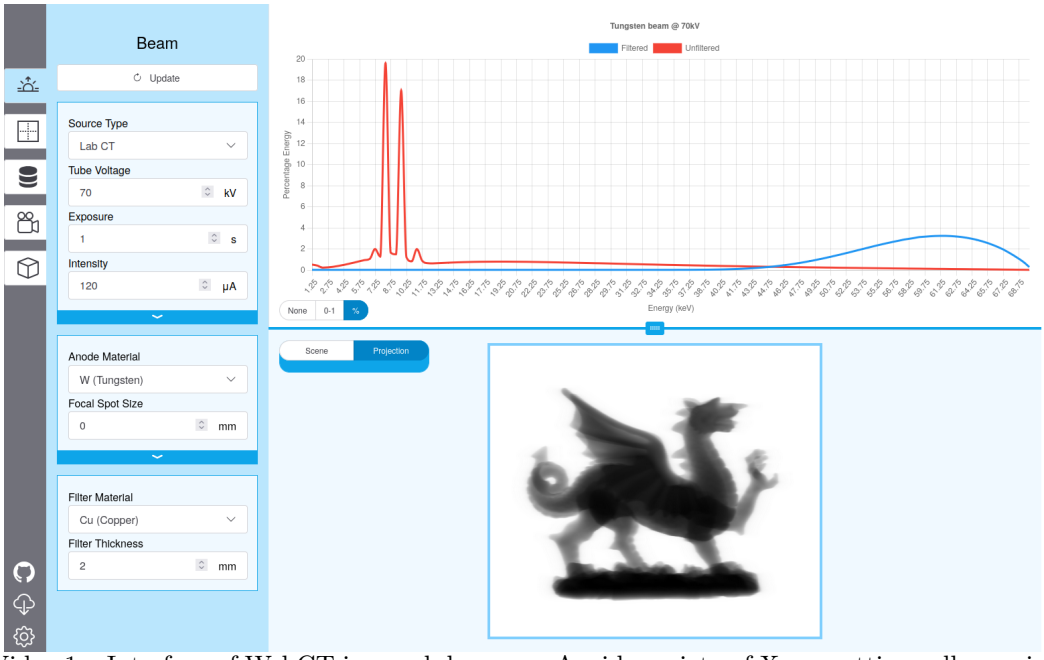

Figure 1: Video 1 – Interface of WebCT in a web browser. A wide variety of X-ray settings allow quick, iterative scan planning and training. https://youtu.be/KZRkw_p0xbA

slices are close to each other. Hounsfield values are comparable. MAPE is about 5% and the ZNCC is above 98%, indicating a high level of correlation between the two volumes. The errors are more due to segmentation inaccuracies and noise than the simulation implementation itself. Indeed, when simulated X-ray projections are compared with digitally reconstructed radiographs (DRRs) computed from the experimental CT scan, ZNCC is 99.66%, which is close to 100%; SSIM is 0.98, which is close to 1; and MAPE is 1.76%, which is close to 0%.

gVXR is so fast that it is possible to embed the X-ray simulation into objective functions and register a simulated radiograph on experimental data (see Figure 18). A real digital radiograph was taken with a clinical X-ray machine by GE Healthcare (Chicago, Illinois, USA) at Ysbyty Gwynedd Hospital. The digital Lungman phantom was registered to reproduce the same position and orientation as in the digital radiography taken with the clinical device. ZNCC is 98.91%, SSIM is 0.94, and MAPE is 1.56%. It demonstrates the ability of gVXR to reproduce radiographs taken with clinically utilized devices.

4. APPLICATIONS

4.1 Digital twinning

Digital Twinning is the creation of virtual models of real-life components. In this case, gVirtualXray allows true representative X-ray simulations calibrated to real-life machines. To create a Digital Twin, all factors of an X-ray system must be taken into account, ranging from the mechanics of the system (can the detector or source move? What clearance is available for the sample?, etc) to X-ray source and detector properties (maximum kV, focal spot size, pixel resolution, scintillator properties, PSF, and so forth). A core part of creating a Digital Twin is calibrating the noise of a system based on the target amperage, this involves an experimental method to measure the noise characteristics at differing mAs values, which then can be exposed in the model as a parameter to users of the Virtual Twin.

gVirtualXray's flexible API has allowed the development of WebCT (https://webct.io/, accessed: 18 Jul 2024), an interactive real-time web-based app for X-ray simulation, allowing anyone of any skill level to quickly simulate an X-ray scanner (see Figure 1). This is excellent for scan planning, answering feasibility questions, and teaching/training on X-ray systems without requiring access to expensive equipment.

We are developing digital twins of specific beamlines, including selected laboratory computed tomography (labCT) devices and a synchrotron. One of them is a new dual-beam XRCT laboratory equipment of the MateIS laboratory (Lyon, France).[20] The noise model is under validation and a specific dual-beam calibration protocol has been proposed.[21] We report here the acquisition and simulation of an aluminum component of a tensile machine for in situ stress in scanning electron microscopes (SEM) because a CAD model is available. The most significant data acquisition parameters used during the experiment were inputed in gVXR. Simulated X-ray projections of the CAD model are registered onto the experimental one (see Figure 18). Figure 2 shows a great level of similarity between images acquired with the actual device and its digital twin. All the artifacts visible in slices reconstructed from experimental data are also visible in the simulated ones (see Figure 3).

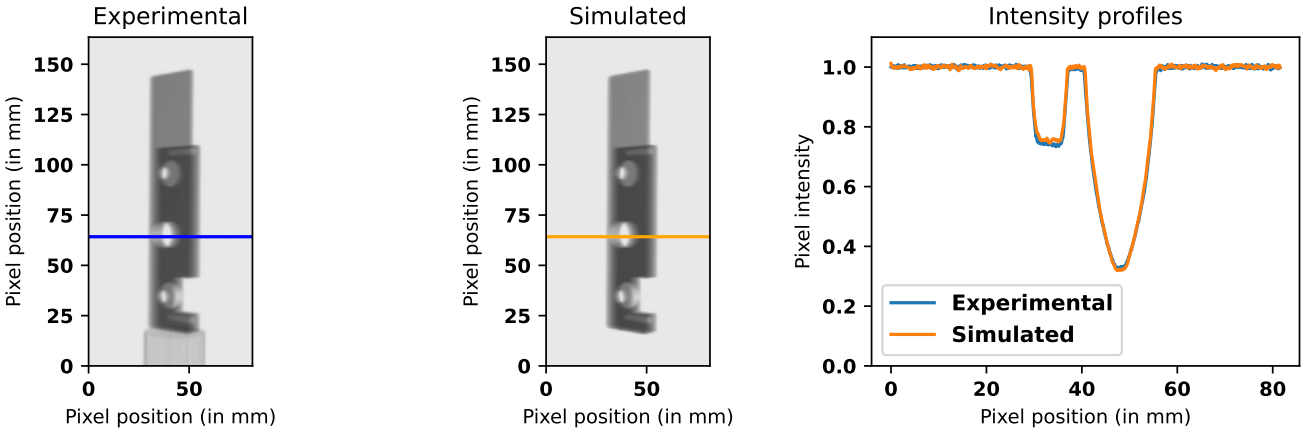

Figure 2: Comparison between X-ray projections taken with a real dual-beam XRCT laboratory device and its digital twin. For fair comparison, both projections are displayed using the same lookup table.

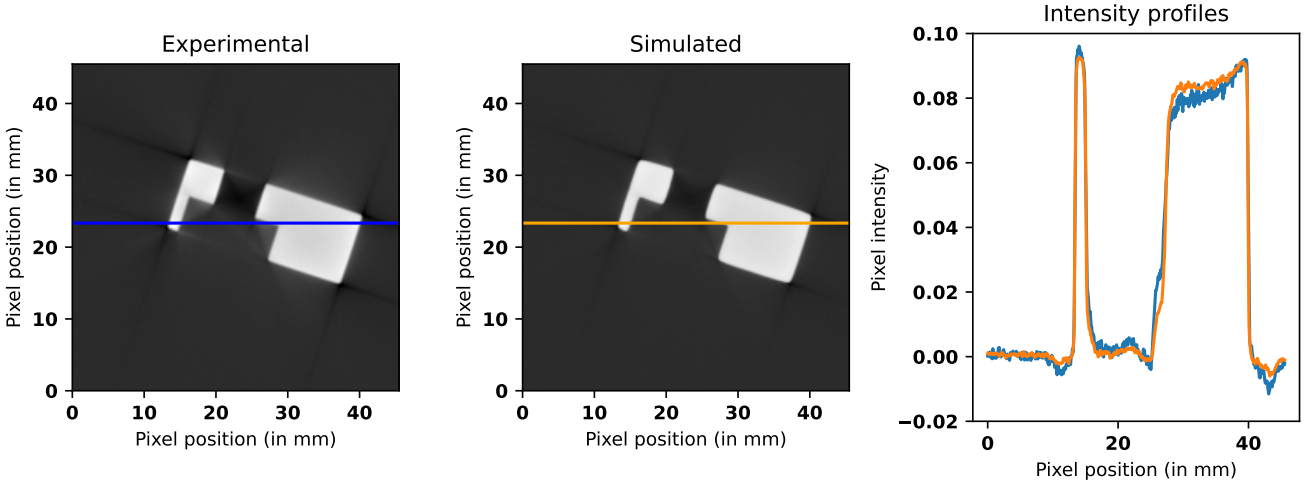

Figure 3: Comparison between CT slices reconstructed from data taken with a real dual-beam XRCT laboratory device and its digital twin. For fair comparison, both slices are displayed using the same lookup table.

We are also building a predictive tool for synchrotron µ-CT at the Dual Imaging And Diffraction (DIAD) beamline of the Diamond Light Source[22] and integrating it in gVXR. DIAD is a dual-beam X-ray instrument for quasi-simultaneous imaging and diffraction, which operates two independent beams at energies of 7-38 keV. Such digital twins will be integrated into gVXR and made available to any user in WebCT.

The development of such digital twins opens up new perspectives, it is now possible:

- To train users on specific devices;
- To predict what experimental data will look like from CAD models;

- To assess the feasibility of scanning specific samples on specific devices before submitting beamtime proposals to facilities;
- To optimize scanning parameters offline, i.e. before beamtime;
- To generate a large amount of automatically annotated data for training machine learning algorithms;
- To design new systems.

4.2 Education

We have deployed gVXR in material science lab-sessions delivered to about 150 MEng students a year at the INSA-Lyon and Polytech Lyon 1 engineer schools. It has been embedded in a Jupyter notebook together with the open-source reconstruction toolkit RTK.[23] Several interactive exercises have been proposed to enable students to learn and gain hands-on experience with X-ray tomographic setups. They first study both digitally with the twin and experimentally with the bench the critical sensibility to crack orientation in a cylindrical sample (additive manufacturing) in which a through crack has been added. Then the students gradually familiarize themselves with the 3D reconstruction technique: (i) first with mono-energy and no noise (i.e. infinite stat), then (ii) with a given exposure (i.e. number of X-rays per pixel) to highlight photon starvation, and (iii) finally with a realistic energy distribution typical of an X-ray generator to understand beam hardening. An example of the 3D visualization of the reconstructed simulated volume is shown in Figure 4. It is worth noting that this progression in the complexity of the imaging setup cannot be done experimentally with such cohort sizes. The digital twinning of the X-ray setup is crucial for those lab sessions of the material science department.

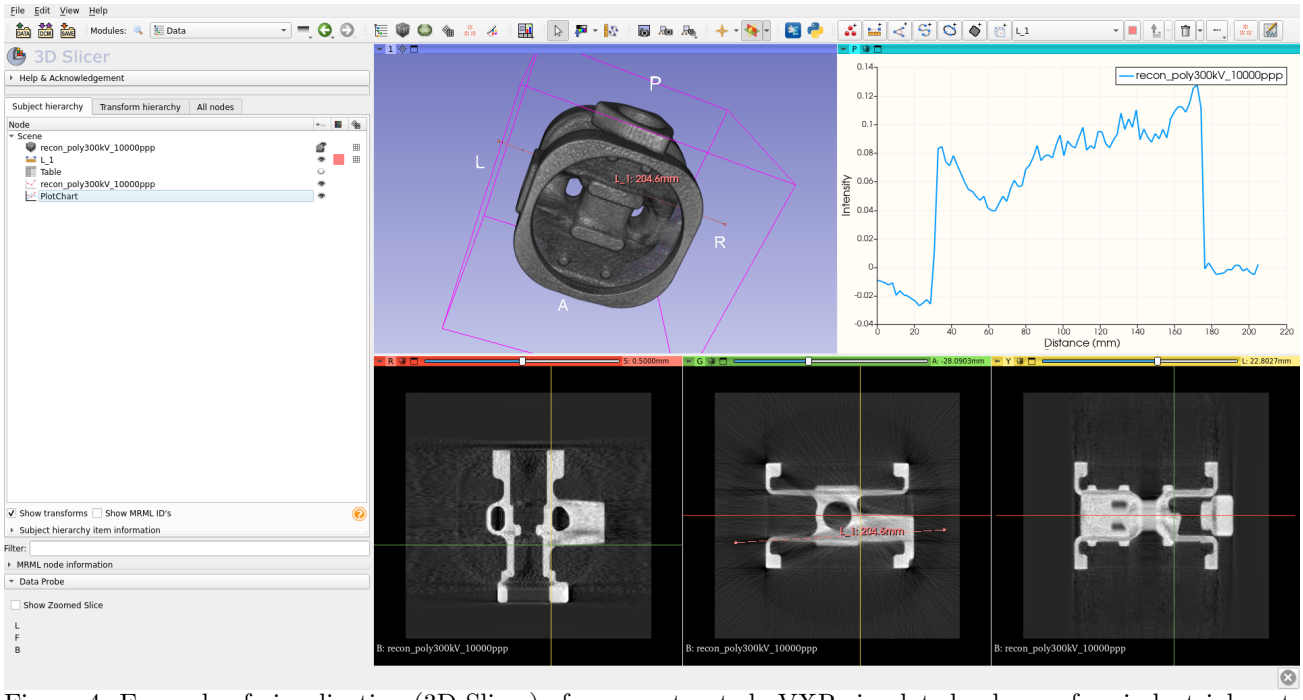

Figure 4: Example of visualization (3D-Slicer) of a reconstructed gVXR-simulated volume of an industrial part: volume rendering, sampled profile in the volume and orthogonal sections.

4.3 Set-up of an experiment

In non-destructive testing (NDT), X-ray computed tomography (CT) is commonly used to find defects in materials. Simulations were performed to ascertain the feasibility of CT scans of ceramic kernels held within a dissimilar ceramic matrix. Ceramic-ceramic matrix composites are garnering a great deal of interest in many applications, including as nuclear fuels for high-temperature gas reactors. The aim is to conduct experiments

i) to detect the interface between two very similar materials (in terms of composition and density), and ii) to assess the defects in the structure that exist as a result of manufacturing methods in spherical ZrB_2 kernels held within a cylindrical zirconium dioxide (ZrO_2) matrix material.

A loss of density compared to theoretical values is expected due to the manufacturing process. Prior to the simulations, samples were produced. The diameter and height of the cylindrical matrix and the diameter of a typical spherical kernel were measured using a caliper. Their masses were assessed using a digital weighing scale. It makes it possible to compute the volume and material densities of the ZrB_2 kernels and the ZrO_2 matrix. This way, we can ensure the simulations are based on realistic values in terms of sizes, densities and material compositions. Table 1 provides a summary of the sample composition.

Table 1: Description of the sample composition.

Material / Properties	Matrix	Kernels
Composition	ZrO_2	ZrB_2
Shape	Cylinder	Spheres
Diameter	8 to 10 mm	0.8 to 1 mm
Height	10 mm	N/A
Theoretical density	5.68 g/cm^3	6.08 g/cm^3
Measured density	3.23 g/cm^3	2.43 g/cm^3
Measured reduction of density	43%	60%

As the materials are close to each other and as the samples are relatively dense, i.e. opaque to X-rays, we will favor synchrotron radiation over the use of conventional X-ray tubes used in labCT. This is because synchrotron radiation can provide almost monochromatic spectra with high flux.

We use the Diamond Light Source, UK's national synchrotron radiation facilities, as an example. Two CT beamlines are available: the low-energy DIAD beamline, and higher-energy I12 beamline. A suitable energy must be selected i) to maximize the contrast between the two materials, and ii) to allow a sufficient level of radiation transmission through the sample. As CT images correspond to maps of linear attenuation coefficients, μ in Eq. 1, we aim at maximizing the difference between the coefficients of zirconium diboride (ZrB_2) and ZrO_2. The difference is the largest for 7 keV. However, when we apply the Beer-Lambert law in Eq. 1 using μ and $\mathbf{d}$ values corresponding to the sample, the transmission through the sample is 0%, i.e. hardly any photon reaches the detector behind the sample. The transmission remains low (below 5%) until roughly 95 keV. At first sight, the issue is that we achieve the best absolute differences at low energies ($\mu_{ZrO_2} - \mu_{ZrB_2}$ in Table 2), but only high energies seem to be suitable to image the sample. Indeed, Table 2 also shows that the transmission remains below 5% until 110 keV. We must therefore ascertain that a difference in attenuation coefficient of 0.39, 0.28, or

Table 2: Theoretical linear attenuation coefficients and photon transmission through the sample at energies supported by the CT beamlines at the Diamond Light Source.

Energy (in keV)	μ_{ZrO_2} (matrix) (in cm^{-1})	μ_{ZrB_2} (kernels) (in cm^{-1})	$\mu_{ZrO_2} - \mu_{ZrB_2}$	$\frac{\mu_{ZrO_2} - \mu_{ZrB_2}}{\mu_{ZrO_2}}$	Transmission
7	479.61	383.02	96.59	20.14%	0.00%
38	31.63	25.84	5.79	18.31%	0.00%
53	12.78	10.42	2.36	18.47%	0.00%
60	9.13	7.43	1.70	18.62%	0.01%
70	6.05	4.91	1.14	18.84%	0.28%
90	3.16	2.55	0.61	19.30%	4.61%
110	1.95	1.56	0.39	20.00%	14.96%
130	1.36	1.07	0.28	20.59%	26.79%
150	1.02	0.80	0.22	21.57%	37.05%

0.22 cm^{-1} is significant enough to be visualized in reconstructed CT scans. The relative difference $(\frac{\mu_{ZrO_2}-\mu_{ZrB_2}}{\mu_{ZrO_2}})$ remains constant $(19.54\% \pm 1.11\%)$ across all the energies, despite both material being close to each other. To select a suitable energy and make sure this relative difference in μ is sufficient enough, we performed simulated CT acquisitions at energies with the ranges [7, 38] and [53, 150] keV supported by the DIAD and I12 beamlines. Photonic noise and a few percent of harmonics were empirically added to the beam spectrum for added realism. Figure 5 shows that according to our initial assumption energies below 85 keV were inappropriate. At 7, 38 and 53 keV, we were not able to scan the sample due to photon starvation. Figure 6 shows CT slices reconstructed from experimental data acquired at the high energy beamline. As expected, no kernel is visible in the experimental images at 70 keV. Again, this is due to photon starvation as transmission is only 0.28%. As expected, 110 keV and 150 keV are suitable energies. However, 150 keV was selected as it can lead to faster scans due to a higher transmission rate.

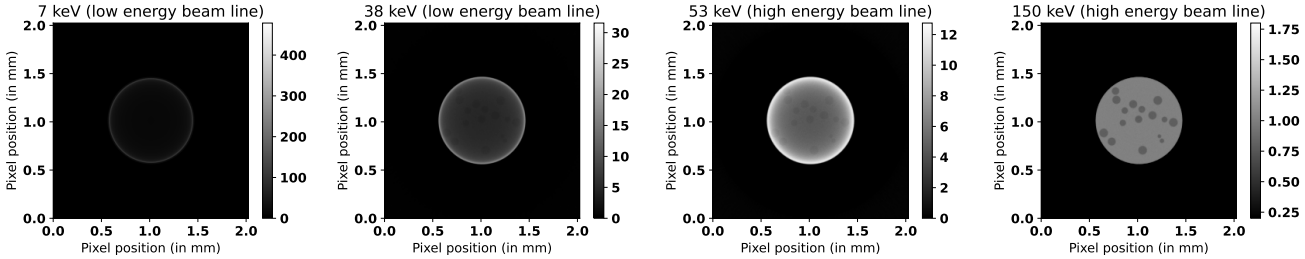

Figure 5: CT slices of mock nuclear fuel reconstructed from simulated data.

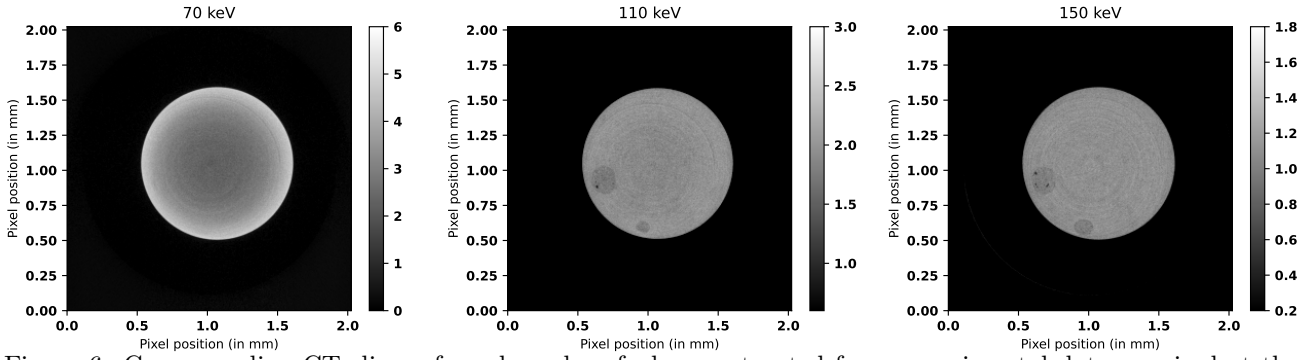

Figure 6: Corresponding CT slices of mock nuclear fuel reconstructed from experimental data acquired at the high energy beamline. The same geometrical set up is used. The only change is the incident energy.

4.4 Machine Learning

4.4.1 Data augmentation for image segmentation

The use of deep learning models has become increasingly common in image analysis, particularly for detection, classification and segmentation tasks. To effectively train these diagnostic tools, a large database of labeled images is required to prevent overfitting and promote model generalization. Collecting these samples is a major obstacle due to the time, money, and human resources required to acquire labeled images, as well as data anonymization requirements.[24] To improve the performance of these diagnostic tools, various data augmentation strategies have been developed to generate synthetic images along with their corresponding labels. The most common method is the use of generative networks.[25] However, generative networks have limitations, including the need for a large database for training and often limited generalization capabilities.[26]

The combined use of a virtual anthropomorphic model with gVirtualXray in clinical imaging would allow the rapid generation of a large dataset of labeled synthetic images. This method allows the injection of artificial lesions into the virtual model, as well as the deformation of organ shapes and the modification of scanner settings to replicate the variability found in real datasets. This approach is used for both conventional X-ray tomography as well as spectral imaging.

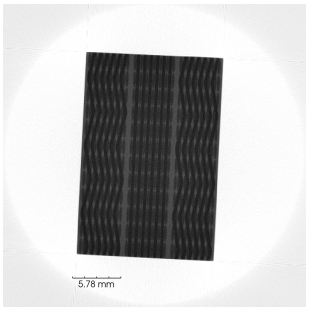

(a) A simulated tomographic slice.

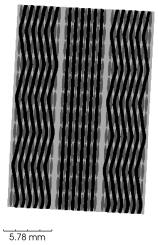

(b) The slice in (a) segmented in to air, weft yarns, warp yarns, and pure matrix.

Figure 7: A tomographic slice of a virtual recreation of a woven carbon fiber reinforced woven composite (a) is shown next to its corresponding voxelization, i.e segmentation ground truth (b).

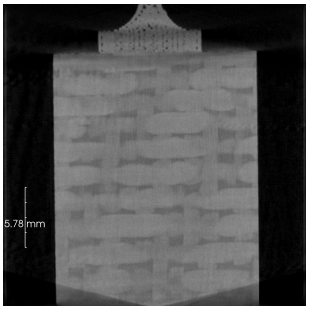

(a) A tomographic slice of a woven carbon fiber reinforced polymer sample.

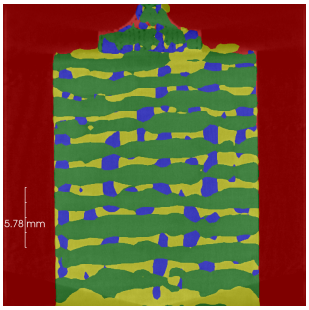

(b) A machine learning derived segmentation. Air is shown in red, weft yarns in blue, warp yarns in green, and pure matrix is shown in yellow.

Figure 8: A tomographic slice of a carbon fiber reinforced polymer woven composite (a) is shown together with a machine learning derived segmentation (b).

The applicability of gVirtualXray for synthetic training data generation in material science is demonstrated by training DeepLabV3 with a Resnet50 backbone using simulated tomograms.[27] The geometries to be scanned are generated with the open source software TexGen.[28] The segmented ground truths are received by voxelizing the input surface meshes in the same frame of reference as the simulated scan is performed. This is shown in Figure 7. The model is trained on 30 synthetic tomograms, where the scan settings and geometry have been domain randomized. Inference on an experimentally derived (not-simulated) tomographic slice is shown in Figure 8. This initial test shows promise, and it is likely a larger dataset and better tuned training procedure will yield better performance.

4.4.2 Defect detection and characterization

In another material science application, gVirtualXray is used to automatically detect and characterize damages in composite and laminate materials by deploying it in data-driven predictor models. It has been evaluated for different specimens under test, structure geometries, materials, and defects. They pose different coincidences between material (defect) and image features:

1. Homogeneous aluminum die casting plates with pore defects[29]
2. Composite Fibre-Metal laminate plates (FML, aluminum and PREG layers with impact damages posing layer delaminations, deformation, cracks, and kissing bond defects (loss of adhesive contact between layers).

Automated feature detection and marking in measuring images can occur on different levels:

- Region-of-Interest search;

- Feature marking and maps;
- Damage and defect classification;
- Damage and defect localization;
- Global statistical aggregates (e.g., pore density, defect distribution).

One of the major issues in data-driven modeling in materials science is the low variance of data with respect to the parameter space. The number of features in measuring data is often limited. For example, impact damages, breakage defects, or tensile tests can only be applied once to a specimen. To overcome the limitation of the sparse experimental parameter space, simulation of measuring data (e.g., X-ray images) using parameterizable mechanical models should be used. The mechanical model is used for the X-ray image simulation. The model consists of geometric objects with different material densities. Constructive Solid Geometry (CSG) modeling is used to create complex 3-dim bodies. CSG consists of additive and subtractive Boolean operations combining shapes. A subtractive operation assumes a host material and a tool shape, e.g., using cylinders for creating holes. We are using the OpenSCAD tool[30] to create triangular mesh-grid models (STL format) that are processed by gVXR. Multi-material parts are imported with multiple STL files, each file is associated with a material density. All parts are merged internally with the respective material density. The basic CSG-CAD model for a plate with pores is shown in Figure 9. Monte Carlo simulation is used to provide random distributions of locations, sizes, and orientations of pores. Pores will reduce the total material density along an X-ray path, resulting in brighter areas. The gVXR-based xraysim tool was used to create X-ray radiography images (1024 × 1024 pixels), finally overlayed with Gaussian distributed random noise (average SNR=2 with respect to the pore intensity variation). Examples of noisy X-ray images and the output of the feature marking machine learning (ML) model are shown in Figure 10. In contrast to the pore analysis use-case, impact damage analysis is still a challenge[31] and a work in progress.

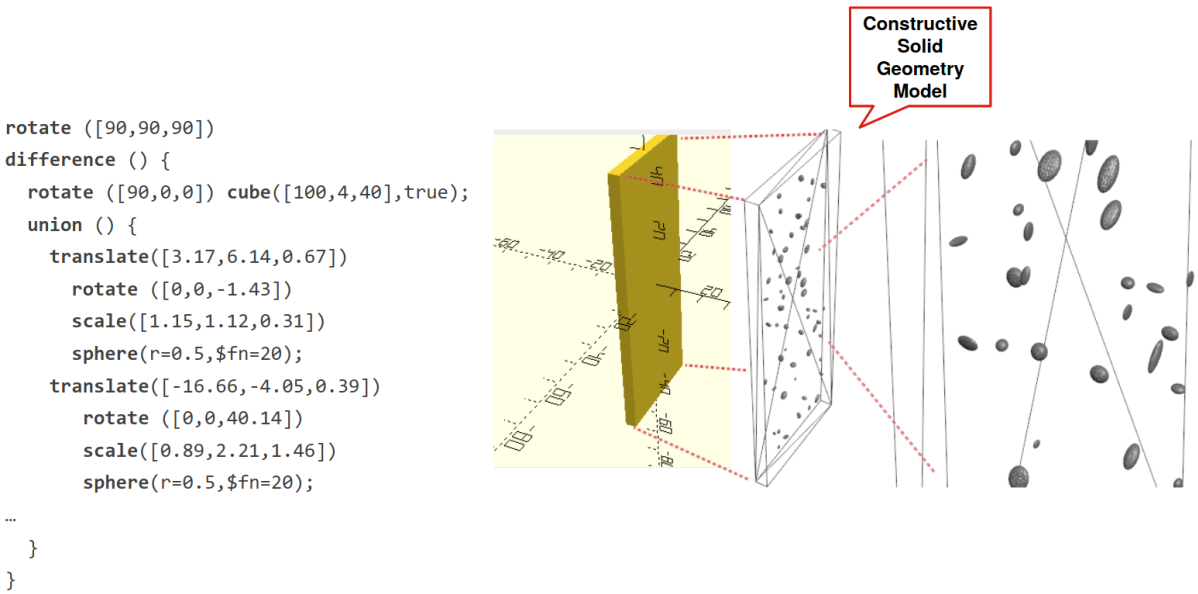

Figure 9: CSG-CAD model of a plate with pores

4.4.3 Characterization of surface roughness for additive manufacturing

This project investigates the use of deep learning (DL) as a tool to quickly determine where the "real" surface is in a reconstructed XCT image with a good level of precision. To do so, synthetic virtual rough surfaces were created to obtain the "ground truth" data (Figure 11a) using a newly developed plugin written in ImageJ macro language. The macro allows the generation of a cuboid hollow shape presenting various surface roughness (Figure 11b).

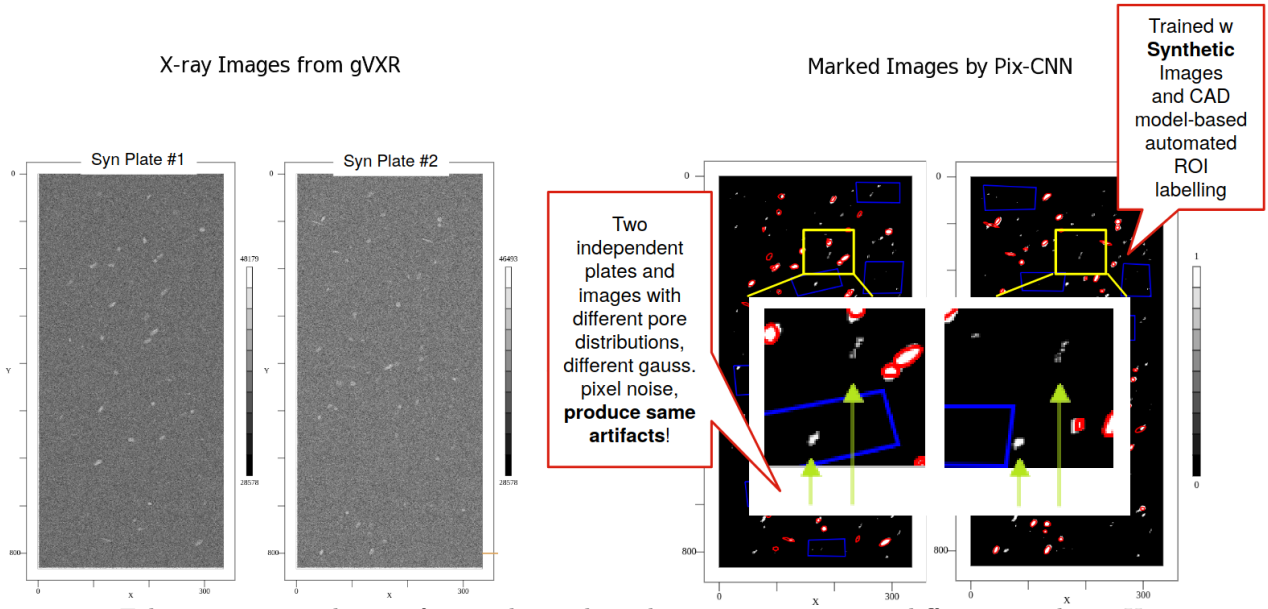

Figure 10: False-positive markings of pores located at the same positions in different synthetic X-ray images with different specimens.

These cuboids were successively virtually scanned using X-ray simulation code gVirtualXray. Using simulations to generate virtual scans and data provided several advantages over real experimental scans: a full CT scan can take several hours to complete, whereas simulations are a time-efficient tool that can rapidly generate data for analysis. The trained neural network demonstrated significant success in improving the resolution of the rough surface images, as evidenced by a relative mean average error on the test data of 1.92% (Figure 12).

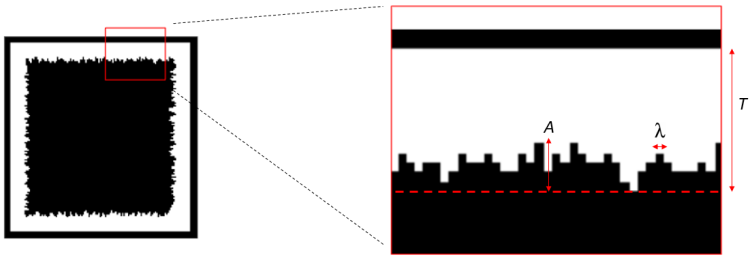

(a) On the left, a "slice" of the cuboid can be seen. In the middle, a zoomed-in section of the surface is shown, with the A being the amplitude, I the wavelength and T the thickness. The dashed red line is the baseline from which the rough surface was constructed.

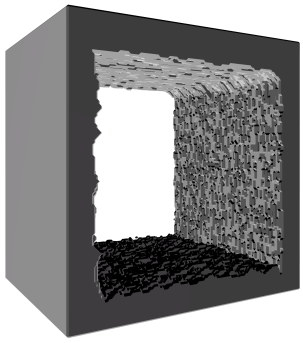

(b) Three-dimensional representation of one of the cuboids.

Figure 11: Synthetic data created by the software.

4.5 Simulations in the objective function of an optimization algorithm

4.5.1 Focal spot assessment

In the industry of non-destructive testing, common X-ray generating devices consist of a wire-cathode emitting an electron beam which is accelerated towards an anode. The scattering of electrons on the anode causes the emission of X-rays via the bremsstrahlung, Auger and X-ray fluorescence effects.[32] This type of device can be relatively compact and is therefore well-suited for industrial applications. However, this type of device suffers from some image blurring as the electron beam impacts the anode on a non-punctual area; creating a focal

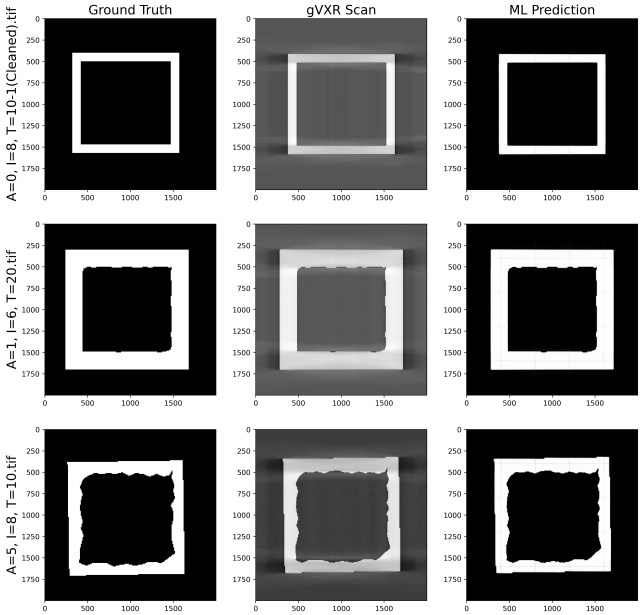

Figure 12: Comparison of the ground truth, gVXR scan and neural network prediction for 3 different cube slices: the cube parameters are shown at the left of each ground truth image. The x and y axes are labeled with the pixel numbers.

spot. Controlling the size and shape of the focal spot is an important challenge as nowadays non-destructive testing and dimensional measurements require spatial resolution in the micrometer range.[33–35] Achieving spatial resolution of the order of the micrometer requires small focal spot sizes and large magnification factors, resulting in low X-ray flux; thus impeding the ability to scan thick mechanical pieces in a reasonable time frame. The X-ray flux may be increased by increasing the applied current, but usually at the expense of a larger focal spot size, and a consecutive loss in spatial resolution.[32]

In this context, deconvolution techniques are a promising and full software solution for retrieving sharp X-ray images from blurred ones. Indeed, new deconvolution techniques have been rapidly developing last decade[36,37] and offer the possibility to use devices with large focal spots, while generating images with sufficient resolution. However, deconvolution techniques require the knowledge of the shape of the focal spot, or PSF. Numerous techniques exist for determining the PSF of a CT device, such as pin-hole camera, line and edge profiles,[38] spheres[39] and other phantoms.[40]

We propose to estimate 2D PSFs of a CT device from 2D images of tungsten sphere phantoms. Given a 2D experimental image of a tungsten sphere, a sharp theoretical 2D X-ray image with a punctual focal spot is generated using gVXR. The corresponding PSF h is then estimated from the two theoretical x and experimental y images using a Richardson-Lucy[41,42] algorithm along with a total variation (TV) regularization.[43]As proposed by Engelhardt and Baumann,[44] the idea is to retrieve the PSF by inversion of a convolution process, where the experimental image is regarded as the blurred version of the theoretical image. A robust optimization procedure is performed using the simplex method[45] for taking into account the uncertainties on the position of the sphere with respect to the X-ray source. The optimization procedure is depicted in Figure 13. gVXR plays a central role as it generates a new theoretical image $x(P)$ for each new guessed sphere's position P during this optimization procedure. Especially, the fact that gVXR is fast in generating an X-ray image allows it to run the optimization within a reasonable time frame.

Figure 14 schematizes the experimental set-up. Experimental images of a $1mm$ tungsten sphere were acquired at different voltages and currents (see Figure 15). The X-ray generator is a *Comet MXR 320 HP 11 FB 90* with two focal spots of $0.4\,mm$ and $1.0\,mm$. The detector is a *Varex XRD 1620 xN CS* of $41 \times 41\,cm$ with 2048×2048 pixels and a pixel pitch of $200\,\mu m$. The source-to-detector distance (SDD) was $1150\,mm$, while the source to object (a.k.a. the sphere) distance was approximately measured at $90\,mm$.

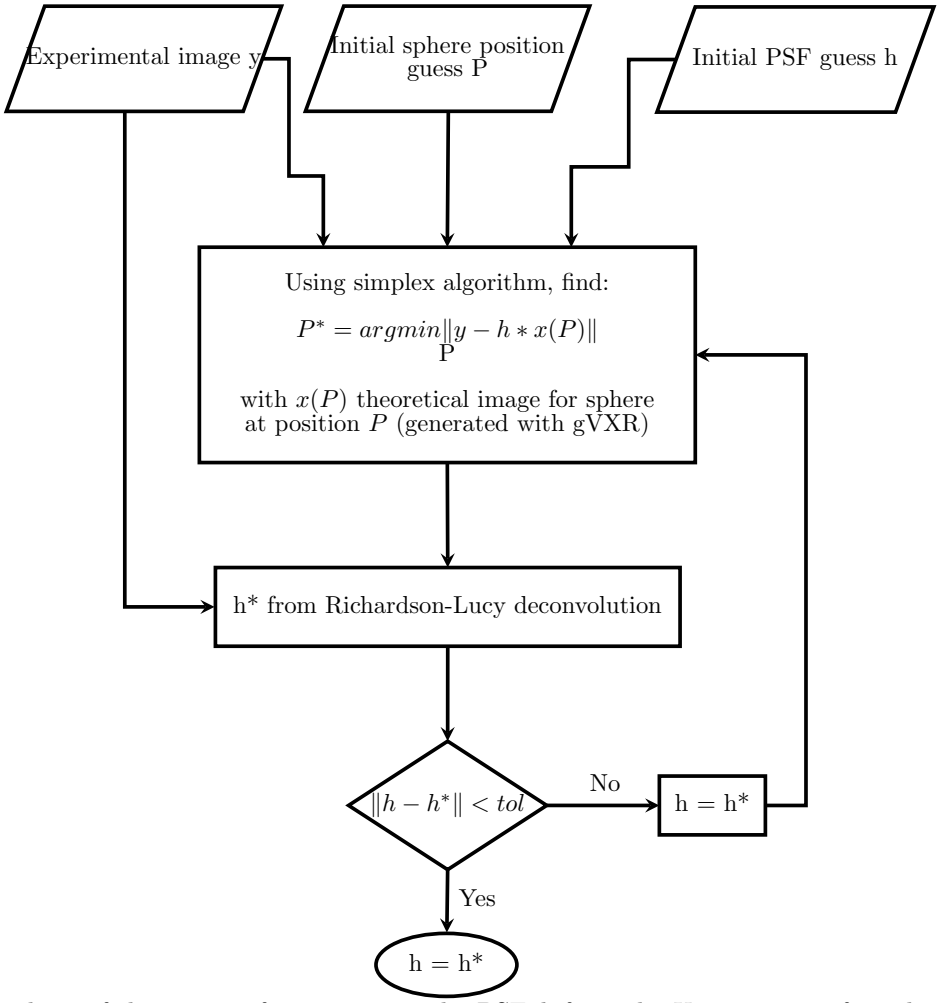

Figure 13: Flow chart of the process for estimating the PSF h from the X-ray image of a sphere. See text for details.

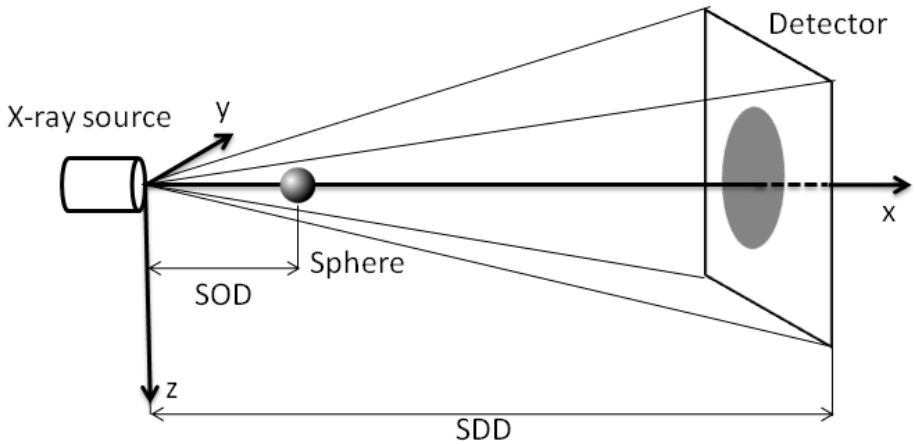

Figure 14: Schematic of the experimental set-up for acquiring the X-ray image of a tungsten sphere.

Figure 16 shows the corresponding estimated PSFs to the acquired X-ray sphere images of Figure 15 using the algorithm described in Figure 13. Figure 17 displays the corresponding deblurred spheres of Figure 15 using their related estimated PSFs of Figure 16 through the "fast total variation deconvolution" algorithm.[46]

(a) $100\,kV$ at $650\,\mu A$, $0.4\,mm$ focal spot. (b) $240\,kV$ at $7500\,\mu A$, $1.0\,mm$ focal spot.

Figure 15: Acquired X-ray images of a $1\,mm$ tungsten sphere at different voltages, currents and focal spots sizes using a *Comet MXR 320 HP 11 FB 90* tube. Note: for visualization purposes, images were cropped and contrast enhanced.

(a) $100\,kV$ at $650\,\mu A$, $0.4\,mm$ focal spot. (b) $240\,kV$ at $7500\,\mu A$, $1.0\,mm$ focal spot.

Figure 16: Corresponding 81×81 pixels PSFs estimated to the X-ray sphere images shown in Figure 15.

(a) $100\,kV$ at $650\,\mu A$, $0.4\,mm$ focal spot. (b) $240\,kV$ at $7500\,\mu A$, $1.0\,mm$ focal spot.

Figure 17: Deblurred spheres of Figure 15, using corresponding estimated PSFs of Figure 16. Note: for visualization purposes, images were cropped and contrast enhanced.

4.5.2 Comparison of a manufactured object with its original CAD design

When a scanned object is manufactured from CAD, it is possible to register simulated projections of the CAD model onto the X-ray projections taken during a CT scan acquisition. An optimization algorithm iteratively tweaks the position and orientation of the CAD model until the differences between the simulated and the experimental projections are minimized. Figure 18 illustrates the whole process. We show here the results on an optical component (mirror petal) for a nanosatellite (< 10 kg) produced with additive manufacturing (AM) (see Figure 19),[47] but the technique has been applied on other samples. After registration, we have a perfect geometrical alignment of the simulated CAD model and the object in the CT device. It makes it possible to

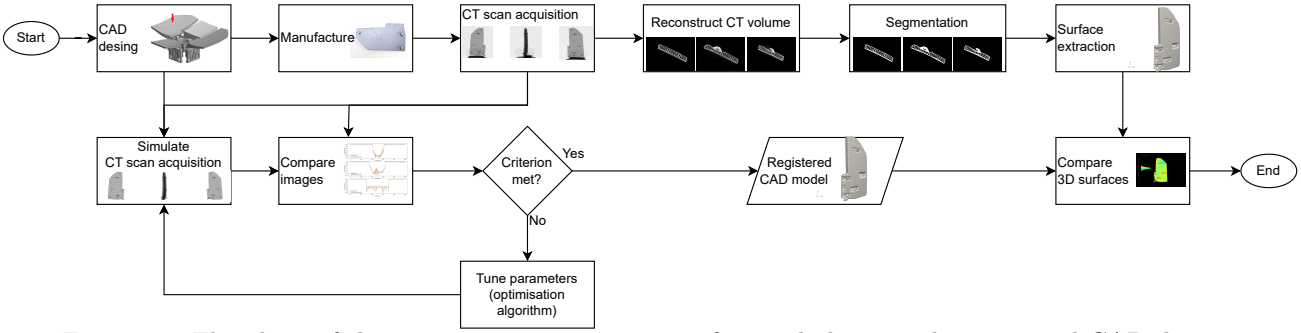

Figure 18: Flowchart of the process to compare a manufactured object with its original CAD design.

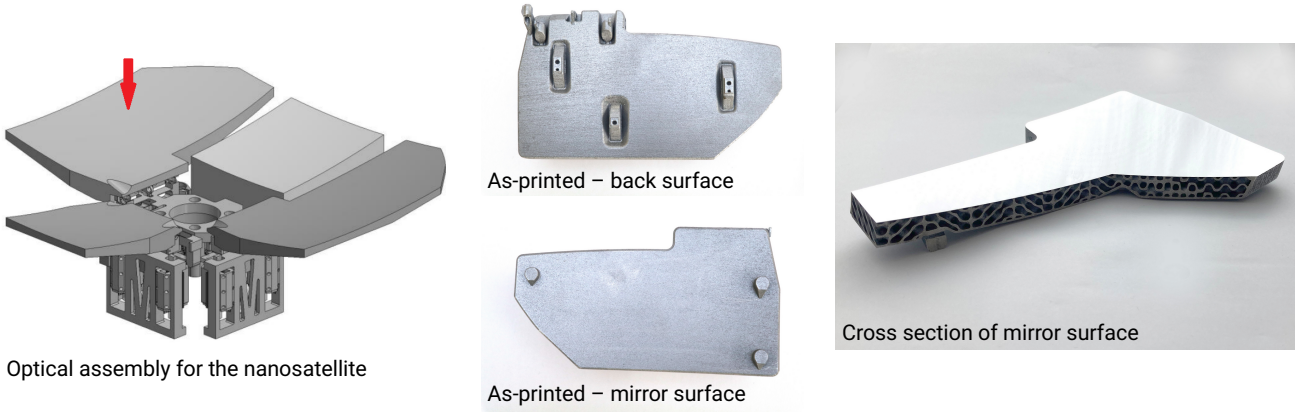

Figure 19: (left) the nanosatellite optical assembly highlighting the mirror petal; (middle) the as-printed design that underwent XCT acquisition; and (right) a cross section through the reflective surface showing the internal lattice.

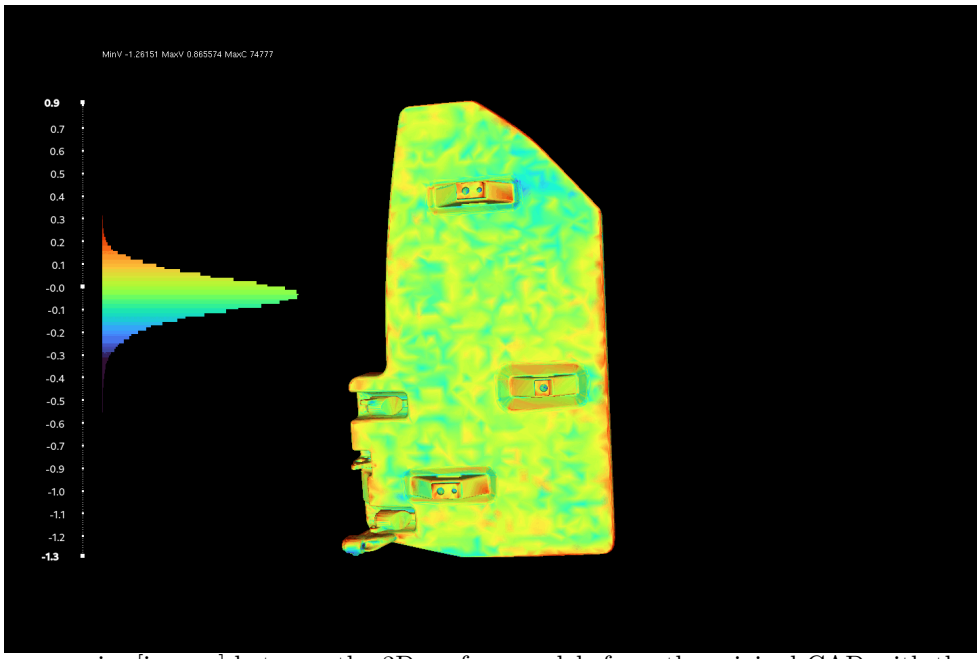

Figure 20: Discrepancies [in mm] between the 3D surface models from the original CAD with the one extracted from the segmentation of the experimental scan.

visually compare and quantify differences between the 3D surface models from the original CAD with the one extracted from the segmentation of the experimental scan (see Figure 20). The color used in the visualization is related to the error, making it easy to identify where the sample is smaller or larger than the CAD model.

4.5.3 Assessment and optimization of industrial XCT performance

The performance of an XCT scan depends on many factors. Furthermore, the performance of an XCT scan is likely to vary across the reconstructed volume of a given component. For example, in NDT for industrial components using polychromatic sources, the contrast generated by a defect in the part is expected to vary depending on the amount of material being penetrated across each projection in the scan.

While the performance will clearly be affected by modifying the X-ray source parameters and modifying the pose of the part, it is difficult to gain a good understanding of the spatial variability of the inspection performance for a given setup without running a significant experimental campaign utilizing a large number of samples with defects deliberately seeded at specific locations. However, experimental testing can be unattractive, not only due to associated high cost and material waste, but it requires the development to be mature enough for component manufacturing. This is often not the case for newly developing products, and often the design may need to be re-iterated, and sometimes re-designed to alleviate any identified inspection challenges.

The MTC has developed a Python framework to automatically configure gVXR setups, seed defect geometries into a part, and track the positions and orientations of these defects in 3D space as the part is reoriented. From this, defect positions in each projection and the reconstructed volume are also computed, which will become important in the calculation of an objective function that aims to maximize the Inspection Performance Map[48] at defect locations.

The part geometry used was the Digital Reconfigurable Additive Manufacturing facilities for Aerospace (DRAMA) additively manufactured $250 \times 15 \times 70$ mm aerofoil in Ti-6Al-4V with laser powder bed fusion. The system being modelled was based on a diondo d2 system, with a 225 kV source and a 400 mm by 400 mm detector, shown in Figure 21.

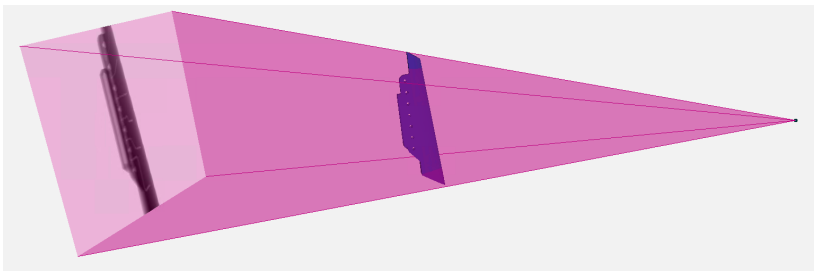

(a) The arrangement of the part with respect to the source and detector. Note that the 3D visualization is a built-in feature of gVXR. It can be used interactively.

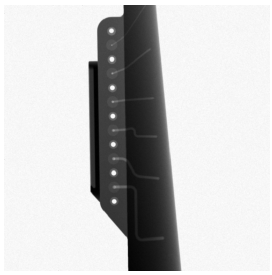

(b) The initial projection.

Figure 21: The initial simulation setup for the DRAMA aerofoil blade component, prior to optimization.

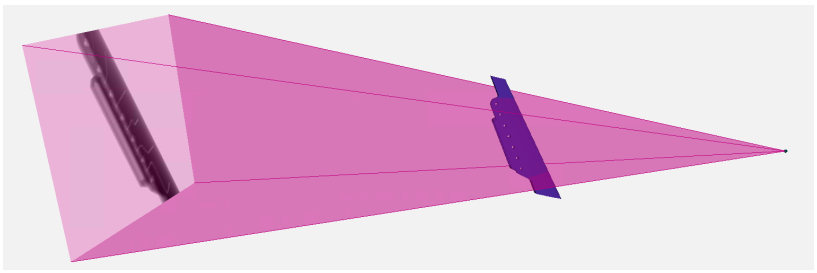

(a) The arrangement of the part with respect to the source and detector.

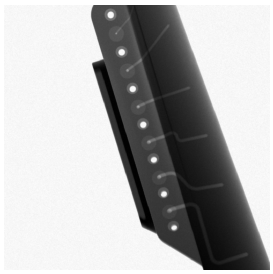

(b) The initial projection.

Figure 22: The initial simulation setup for the DRAMA aerofoil blade component, after optimization.

The final simplex used by the Nelder-Mead optimizer spanned less than 0.5 degrees across the rotational parameters, less than 0.5 mm in the translational offsets, and approximately 1 mm for the source-to-object

distance parameter. The best setup found is shown in Figure 22. Figure 23 shows defect indications evaluated at each position, where it can be seen that the defect indications appear significantly improved, both in magnification and contrast. The most notable change between the initial and optimized setup is that the magnification has been increased to focus the scan on the bracket section. Additionally, the aerofoil has been tilted slightly, which explores the trade-off of incurring slightly longer material path lengths across the part (reducing performance), at the benefit of reducing the vertical extent of the bracket to increase magnification (increasing performance). It can be seen that the tip section of the bracket region lies outside of the scan. This is because the optimizer did not check that all parts of the bracket were in the field of view (only the 7 positions were checked) but in future, more points along the outer extent of the region of interest should be factored into this field of view check.

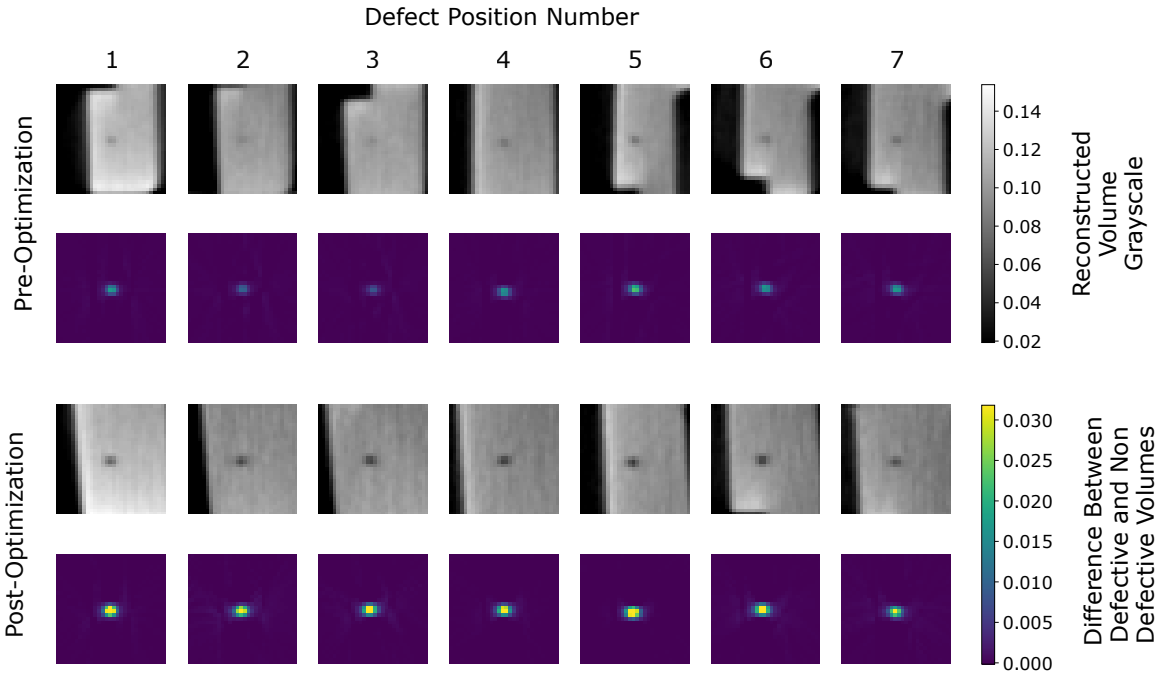

Figure 23: Defect indications for the seven positions before and after optimization. The grayscale range used for plotting is identical across all of the reconstructed volume patches. The grayscale range used for plotting the difference volume patches is also identical across all different images.

5. CONCLUSION

This paper presents gVXR, an open-source framework for simulating X-ray images in real time using GPUs. We have demonstrated gVXR's versatility and applicability across various domains, including education, experimental setup optimization, digital twinning, machine learning, non-destructive testing, and materials science. Extensive validation efforts, including comparisons with Monte Carlo simulations and real experimental data, have confirmed the accuracy of gVXR's simulations. The framework's ability to rapidly generate verifiably accurate X-ray simulations enables researchers and practitioners to explore complex scenarios, optimize experimental parameters, and develop novel approaches in X-ray imaging and analysis. As gVXR continues to evolve, potential areas for future development include improved scatter estimation and enhanced support for spectral imaging. The open-source nature of gVXR enables collaboration and innovation, encouraging future advancements in X-ray simulation and analysis across multiple disciplines.

ACKNOWLEDGMENTS

The development of gVirtualXray is currently supported by the Ada Lovelace Centre. It was initially co-funded by the European Union through the FP7-PEOPLE-2012-CIG - Marie-Curie Action 'Fly Algorithm in PET

Reconstruction for Radiotherapy Treatment Planning' under grant # 321968). F. Vidal thanks NVIDIA Corporation for the donation of the NVIDIA TITAN Xp GPU used in the development and validation of gVirtualXray. F. Vidal, I. Mitchell and S. Middleburgh acknowledge the Diamond Light Source for beamtime # MG29820 on 'Real experiments, hi-fidelity simulations, machine learning and GPUs: Toward the virtual design of nuclear fuel rods'. I. Mitchell and F. Vidal would like to thank Taith for a travel grant awarded to Vidal and Mitchell that made it possible to develop the digital twin of the new dual-beam XRCT laboratory equipment of the MateIS laboratory (Lyon, France). Y. Chahid and C. Atkins acknowledge the UKRI Future Leaders Fellowship 'Printing the future of space telescopes' under grant # MR/T042230/1. J. Friemann acknowledges funding from Horizon Europe through the MSCA Doctoral Network RELIANCE, grant # 101073040. A. Garbout, M. Puig, and H. Lipscomb acknowledges support from the National Research Facility for Lab X-ray CT (NXCT), funded through EPSRC grants # EP/T02593X/1 and # EP/V035932/1 R. Culver acknowledges the 'DRAMA (Digital Reconfigurable Additive Manufacturing facilities for Aerospace)' project funded by UKRI under grant # 113157.

REFERENCES

[1] Duvauchelle, P., Freud, N., Kaftandjian, V., and Babot, D., "A computer code to simulate x-ray imaging techniques," *Nuclear Instruments and Methods in Physics Research Section B: Beam Interactions with Materials and Atoms* **170**(1), 245–258 (2000).

[2] Vidal, F. P., Garnier, M., Freud, N., Létang, J. M., and John, N. W., "Simulation of x-ray attenuation on the GPU," in [*Proceedings of Theory and Practice of Computer Graphics 2009*], 25–32, Eurographics Association, Cardiff, UK (June 2009).

[3] Vidal, F. P. and Villard, P.-F., "Development and validation of real-time simulation of x-ray imaging with respiratory motion," *Computerized Medical Imaging and Graphics* **49**, 1–15 (2016).

[4] Freud, N., Duvauchelle, P., Létang, J. M., and Babot, D., "Fast and robust ray casting algorithms for virtual x-ray imaging," *Nuclear Instruments and Methods in Physics Research Section B: Beam Interactions with Materials and Atoms* **248**(1), 175–180 (2006).

[5] Villard, P.-F., Vidal, F. P., Hunt, C., Bello, F., John, N. W., Johnson, S., and Gould, D. A., "A prototype percutaneous transhepatic cholangiography training simulator with real-time breathing motion," *International Journal of Computer Assisted Radiology and Surgery* **4**(6), 571–578 (2009).

[6] Vidal, F. P., Garnier, M., Freud, N., Létang, J. M., and John, N. W., "Accelerated deterministic simulation of x-ray attenuation using graphics hardware," in [*Eurographics 2010 - Poster*], Poster 5011, Eurographics Association, Norrköping, Sweden (May 2010).

[7] Vidal, F. P., Mitchell, I. T., and Létang, J. M., "Use of fast realistic simulations on GPU to extract CAD models from microtomographic data in the presence of strong CT artefacts," *Precision Engineering* **74**, 110–125 (2022).

[8] Pointon, J. L., Wen, T., Tugwell-Allsup, J., Sújar, A., Létang, J. M., and Vidal, F. P., "Simulation of x-ray projections on gpu: Benchmarking gvirtualxray with clinically realistic phantoms," *Computer Methods and Programs in Biomedicine* **234**, 107500 (2023).

[9] Corbi, A., Burgos, D., Vidal, F., Albiol, F., and Albiol, A., "X-ray imaging virtual online laboratory for engineering undergraduates," *European Journal of Physics* **41**, 014001 (Dec. 2019).

[10] Schoonjans, T., Brunetti, A., Golosio, B., Sanchez del Rio, M., Solé, V. A., Ferrero, C., and Vincze, L., "The xraylib library for x-ray–matter interactions. recent developments," *Spectrochimica Acta Part B: Atomic Spectroscopy* **66**(11), 776–784 (2011).

[11] Poludniowski, G., Omar, A., Bujila, R., and Andreo, P., "Technical note: SpekPy v2.0—a software toolkit for modeling x-ray tube spectra," *Medical Physics* **48**(7), 3630–3637 (2021).

[12] Hernández, G. and Fernández, F., "A model of tungsten anode x-ray spectra," *Medical Physics* **43**(8Part1), 4655–4664 (2016).

[13] Jørgensen, J. S., Ametova, E., Burca, G., Fardell, G., Papoutsellis, E., Pasca, E., Thielemans, K., Turner, M., Warr, R., Lionheart, W. R. B., and Withers, P. J., "Core Imaging Library - Part I: a versatile Python framework for tomographic imaging," *Philosophical Transactions of the Royal Society A: Mathematical, Physical and Engineering Sciences* **379**(2204), 20200192 (2021).

[14] Papadimitroulas, P., Erwin, W. D., Iliadou, V., Kostou, T., Loudos, G., and Kagadis, G. C., "A personalized, monte carlo-based method for internal dosimetric evaluation of radiopharmaceuticals in children," *Medical Physics* **45**(8), 3939–3949 (2018).

[15] Rodriguez Perez, S., Marshall, N., Struelens, L., and Bosmans, H., "Characterization and validation of the thorax phantom lungman for dose assessment in chest radiography optimization studies," *Journal of Medical Imaging* **5**, 1 (02 2018).

[16] McCormick, M., Liu, X., Ibanez, L., Jomier, J., and Marion, C., "ITK: enabling reproducible research and open science," *Frontiers in Neuroinformatics* **8**, 13 (2014).

[17] Schroeder, W., Martin, K., and Lorensen, B., [*The Visualization Toolkit – An Object-Oriented Approach To 3D Graphics*], Kitware, Inc., fourth ed. (2006).

[18] Vidal, F. P. and Tugwell-Allsup, J., "CT scans, 3D segmentations, digital radiograph and 3D surfaces of the Lungman phantom." https://doi.org/10.5281/zenodo.10782644 (Mar. 2024). [Accessed 19-07-2024].

[19] Schneider, W., Bortfeld, T., and Schlegel, W., "Correlation between CT numbers and tissue parameters needed for Monte Carlo simulations of clinical dose distributions," *Physics in Medicine & Biology* **45**, 459–478 (Jan. 2000).

[20] Maire, E., Bonnard, G., Adrien, J., Boulnat, X., Létang, J. M., and Lachambre, J., "Dual beam microfocus high-energy tomography: Towards multimodal and faster laboratory experiments," *Tomography of Materials and Structures* **5**, 100030 (June 2024).

[21] Létang, J. M., Lachambre, J., and Maire, E., "Cross-detector scatter issues in dual synchronous tomography: an affine projection correction protocol," *Tomography of Materials and Structures* **6**, 100039 (Sept. 2024).

[22] Reinhard, C., Drakopoulos, M., Ahmed, S. I., Deyhle, H., James, A., Charlesworth, C. M., Burt, M., Sutter, J., Alexander, S., Garland, P., Yates, T., Marshall, R., Kemp, B., Warrick, E., Pueyos, A., Bradnick, B., Nagni, M., Winter, A. D., Filik, J., Basham, M., Wadeson, N., King, O. N. F., Aslani, N., and Dent, A. J., "Beamline K11 DIAD: a new instrument for dual imaging and diffraction at Diamond Light Source," *Journal of Synchrotron Radiation* **28**, 1985–1995 (Nov 2021).

[23] Rit, S., Oliva, M. V., Brousmiche, S., Labarbe, R., Sarrut, D., and Sharp, G. C., "The reconstruction toolkit (rtk), an open-source cone-beam ct reconstruction toolkit based on the insight toolkit (itk)," *Journal of Physics: Conference Series* **489**, 012079 (mar 2014).

[24] Litjens, G., Kooi, T., Bejnordi, B. E., Setio, A. A. A., Ciompi, F., Ghafoorian, M., Van Der Laak, J. A., Van Ginneken, B., and Sánchez, C. I., "A survey on deep learning in medical image analysis," *Medical Image Analysis* **42**, 60–88 (Dec. 2017).

[25] Garcea, F., Serra, A., Lamberti, F., and Morra, L., "Data augmentation for medical imaging: A systematic literature review," *Computers in Biology and Medicine* **152**, 106391 (Jan. 2023).

[26] Osuala, R., Kushibar, K., Garrucho, L., Linardos, A., Szafranowska, Z., Klein, S., Glocker, B., Diaz, O., and Lekadir, K., "Data synthesis and adversarial networks: A review and meta-analysis in cancer imaging," *Medical Image Analysis* **84**, 102704 (Feb. 2023). arXiv:2107.09543 [cs, eess].

[27] Friemann, J., Mikkelsen, L. P., Oddy, C., and Fagerström, M., "Automated generation of labeled synthetic training data for machine learning based segmentation of 3D-woven composites," in [*Proceedings of the 21st European Conference on Composite Materials: Special sessions*], **8**, 333–338 (2024).

[28] Brown, L. and Long, A., "8 - modeling the geometry of textile reinforcements for composites: Texgen," in [*Composite Reinforcements for Optimum Performance (Second Edition)*], Boisse, P., ed., *Woodhead Publishing Series in Composites Science and Engineering*, 237–265, Woodhead Publishing, second edition ed. (2021).

[29] Bosse, S., Lehmhus, D., and Kumar, S., "Automated porosity characterization for aluminum die casting materials using x-ray radiography, synthetic x-ray data augmentation by simulation, and machine learning," *Sensors* **24**(9), 2933 (2024).

[30] "OpenSCAD — openscad.org." https://openscad.org/. [Accessed 15-07-2024].

[31] Shah, C., Bosse, S., and von Hehl, A., "Taxonomy of damage patterns in composite materials, measuring signals, and methods for automated damage diagnostics," *Materials* **15**(13), 4645 (2022).

[32] Toda, H., [*X-Ray CT - Hardware and Software Techniques*], Springer, Singapore (2021).

[33] Uhlman, N., Salamon, M., and Burtzlaff, S., "Components and Methods for Highest Resolution Computed Tomography," *International Symposium on NDT in Aerospace (Fürth, Germany)* **1**, 3–9 (2008).

[34] Kerckhofs, G., Pyka, G., Moesen, M., Van Bael, S., Schrooten, J., and Wevers, M., "High-Resolution Microfocus X-Ray Computed Tomography for 3D Surface Roughness Measurements of Additive Manufactured Porous Materials," *Advanced Engineering Materials* **15**, 153–158 (mar 2013).

[35] Nikishkov, Y., Seon, G., and Makeev, A., "Structural analysis of composites with porosity defects based on X-ray computed tomography," *Journal of Composite Materials* **48**(17), 2131–2144 (2014).

[36] Makarkin, M. and Bratashov, D., "State-of-the-art approaches for image deconvolution problems, including modern deep learning architectures," *Micromachines* **12**(12) (2021).

[37] Zhu, J., Li, K., and Hao, B., "Hybrid variational model based on alternating direction method for image restoration," *Advances in Difference Equations* **2019**(1) (2019).

[38] Kaftandjian, V., Zhu, Y., Roziere, G., Peix, G., and Babot, D., "A Comparison of the Ball, Wire, Edge, and Bar/Space Pattern Techniques for Modulation Transfer Function Measurements of Linear X-Ray Detectors," *Journal of X-Ray Science and Technology* **6**(2), 205–221 (1996).

[39] Lee, C., dong Song, H., and Baek, J., "3D MTF estimation using sphere phantoms for cone-beam computed tomography systems," *Medical Physics* **47**(7), 2838–2851 (2020).

[40] Probst, G. M., Hou, Q., Boeckmans, B., Xiao, Y. S., and Dewulf, W., "Characterization and stability monitoring of X-ray focal spots," *CIRP Annals* **69**(1), 453–456 (2020).

[41] Richardson, W. H., "Bayesian-based iterative method of image restoration∗," *J. Opt. Soc. Am.* **62**, 55–59 (Jan 1972).

[42] Lucy, L. B., "An iterative technique for the rectification of observed distributions," *The Astronomical Journal* **79**, 745 (jun 1974).

[43] Shaked, E., Dolui, S., and Michailovich, O. V., "Regularized richardson-lucy algorithm for reconstruction of poissonian medical images," in [*2011 IEEE International Symposium on Biomedical Imaging: From Nano to Macro*], 1754–1757, IEEE (2011).

[44] Engelhardt, M. and Baumann, J., "Determination of Size and Intensity Distribution of the Focal Spot of a Microfocus X-ray Tube Using Image Processing," *Ecndt* **Th.2.5.4**, 1–13 (2006).

[45] Nelder, J. A. and Mead, R., "A Simplex Method for Function Minimization," *The Computer Journal* **7**, 308–313 (01 1965).

[46] Wang, Y., Yang, J., Yin, W., and Zhang, Y., "A new alternating minimization algorithm for total variation image reconstruction," *SIAM Journal on Imaging Sciences* **1**(3), 248–272 (2008).

[47] Westsik, M., Wells, J. T., Chahid, Y., Morris, K., Milanova, M., Beardsley, M., Harris, M., Ward, L., Alcock, S. G., Nistea, I.-T., Cottarelli, S., Tammas-Williams, S., and Atkins, C., "From design to evaluation of an additively manufactured, lightweight, deployable mirror for Earth observation," in [*Astronomical Optics: Design, Manufacture, and Test of Space and Ground Systems IV*], Hull, T. B., Kim, D., and Hallibert, P., eds., **12677**, 1267704, International Society for Optics and Photonics, SPIE (2023).

[48] Brierley, N., Nye, B., and McGuinness, J., "Mapping the spatial performance variability of an x-ray computed tomography inspection," *NDT & E International* **107**, 102127 (2019).